

The Shape of Dark Matter Halos in Edge-on Galaxies

I. Overview of HI observations

S.P.C. Peters¹, P.C. van der Kruit¹, R.J. Allen², and K.C. Freeman³

¹ Kapteyn Astronomical Institute, University of Groningen, P.O. Box 800, 9700 AV Groningen, The Netherlands
e-mail: s.p.c.peters@astro.rug.nl; vdkruit@astro.rug.nl

² Space Telescope Science Institute, 3700 San Martin Drive, Baltimore, MD 21218, USA
e-mail: rjallen@stsci.edu

³ Research School of Astronomy and Astrophysics, Australian National University, Cotter Road, Weston, ACT 2611, Australia
e-mail: kcf@mso.anu.edu.au

Submitted: 7 March 2013

ABSTRACT

The shape of the dark matter halo of a galaxy offers valuable clues on the physical nature of dark matter. In this series of papers, we model the structure and kinematics of the baryons in edge-on galaxies. The flaring of the HI disk provides a measure of the vertical force field of that disk. In a similar way, the rotation curve provides a measure of the horizontal force field. As the galaxies are at rest, the combination of these two provides all the required ingredients for full hydrostatic models. We use these models to analyze their potential wells as generated by the dark matter halo and its shape. In this first paper, we explain this project in more detail and present the HI observations of our sample of 8 edge-on galaxies. We also argue that self-absorption of the HI has a significant effect in these galaxies.

Key words. galaxies: structure – galaxies: kinematics and dynamics – galaxies: ISM – galaxies: halos – galaxies: fundamental properties

1. Introduction

Dark matter remains one of the most elusive problems in astronomy. Clues of unseen, “dark” matter have been found for over 80 years (e.g. Oort (1932); Zwicky (1933); Karachentsev (1966)). But only since the analysis of rotation curves of galaxies, both through radio and optical, did the problem of dark matter become clear beyond doubt. This seems to have been first realized by Freeman (1970), who notes that, to fully explain the HI rotation curves of M 33 and NGC 300, there is a need for additional, unseen mass, following a very different distribution. Rubin & Ford (1970) note a similar behavior within the optical disk of Andromeda, from emission line radial velocities, where the mass to light ratio (M/L) increases with radius. The concept of dark matter halos was convincingly demonstrated when HI-rotation curves beyond the optical disks failed to show a decline (Rogstad & Shostak 1972; Roberts & Whitehurst 1975; Bosma 1981). The observed flatness of galaxy rotation curves out to very large radial distances, well beyond the optically observable disks, makes the presence of dark matter inevitable. This confirmation of the presence of dark matter as a major component of galaxies is one of the early triumphs of radio interferometry (Monnier & Allen 2012).

The exact nature of dark matter particles remains unclear, although we can infer some of its properties. Three key constraints lie at the basis. The first follows from the small-scale anisotropies in the cosmic microwave background (CMB). The CMB is a relic of the baryon-photon decoupling and as such it is tracing the baryon distribution at that time. The Wilkinson Microwave Anisotropy Probe (WMAP) has shown that the CMB

is remarkably flat, to order order one in 10^5 , implying that the universe at that time was extremely homogeneous (Bennett et al. 2012). This is in strong contrast with the present universe which is, at small scales, very inhomogeneous. The second constraint comes from the large scale structure, as measured from red-shifted galaxies (Sánchez et al. 2006) and the Lyman-alpha forest (McDonald et al. 2006). The rate at which structures formed in the universe, implies a matter density of $1/4 \sim \Omega_m \sim 1/3$, which is far more than can be observed in our local universe. The third constraint comes from Big-Bang nucleosynthesis (BBNS), which explains the primordial abundance ratios of atom species in the universe (Yang et al. 1984; José & Iliadis 2011). A part of the dark matter can be in the form of dense baryonic matter, such as rogue planets and small black holes. BBNS however places a firm upper limit on the maximum baryonic density. To get a consistent ratio with absorbed abundance ratios, it requires the baryon density to be far below the total matter density Ω_m , with value: $\Omega_b < 0.05$.

The universe could not have formed the amount of structure it has, if we only accommodate for the amount of baryonic matter set by BBNS. To fill the difference between the total and baryonic matter densities, we need a particle which is non-baryonic and which cannot interact with photons. The most likely candidates are weakly interacting massive particles (WIMPs) (Steigman & Turner 1985). If these particles were non-relativistic – “cold” – they could have been clumping together before the baryon-photon decoupling. Once baryons decoupled from photons, they could quickly fall into the existing potential wells as generated by the dark matter, giving a kickstart to the formation of structure. So far, the best constraint on the amount of matter is the 9-year results of WMAP, setting

a limit of $\Omega_b h^2 = 0.02223 \pm 0.00033$ on the baryon density and $\Omega_c h^2 = 0.1153 \pm 0.0019$ on cold dark matter (Bennett et al. 2012).

Another interpretation of the dark matter problem is that we are not missing matter, but rather that our understanding of the laws of gravity is incomplete. One solution to this is modified Newtonian dynamics (MOND) (Milgrom 1983). MOND proposes a modification to Newtonian gravity such that, in the limit of the weakest of forces, the actual force g starts to deviate from the Newtonian force g_N as $g = \sqrt{g_N a_0}$. Here a_0 represents a constant acceleration of $a_0 \approx 10^{-10} \text{ m s}^{-2}$. With this simple modification, MOND is capable of reproducing a surprisingly large set of phenomena traditionally credited as evidence for dark matter (Famaey & McGaugh 2012).

Many theories exist, all with their own merits and problems. The only way to find the true solution is by placing additional (observational) constraints. One such constraint would be the detection of the dark matter particle itself. A range of experiments is underway in an attempt to measure the interaction between ordinary and dark matter particles. Potential WIMP-candidate detections have been reported by some experiments, while these have been contradicted with null detections from other experiments. So far, the results are still under debate and more work is required (Freese et al. 2012).

The importance of simulations for dark matter research was already realized early on, when Ostriker & Peebles (1973) noted that spiral galaxies are intrinsically stable only when they are embedded in the potential well created by a dark matter halo. This halo needs to be 1 to 2.5 times as heavy as the disk to maintain stability against bar formation. With hindsight, we know that bars are far more common in galaxies, and as such the halo is not required for stability. Modern day cosmological dark matter simulations predict that dark matter has a significant impact on the formation and evolution of galaxies. The dark matter clumps into halos, which serve as gravitational sinks for baryonic matter to fall into. Once inside, these baryons form the galaxies and other forms of visible structure in the universe. The size and shape of these halos is influenced by the type of dark matter particle and its merger history. As such, getting a grip on the shape of the halo offers a potential constraint on the dark matter model (Davis et al. 1985).

The shape of dark matter halos can be classified by the shape parameter q , using the ratios between the vertical axis c and major axis a , such that $q = c/a$. This divides the potential halo shapes up into three classes: prolate ($q > 1$), oblate ($q < 1$) and spherical ($q \sim 1$). This is, of course, only a simplified version of reality, where we can also expect tri-axial shapes and changes of shape with radius and history (Vera-Ciro 2013). However, for halos with masses $\gtrsim 10^{12.3} h^{-1} M_\odot$ the halos can be adequately described by a single major-to-minor axis ratio (Schneider et al. 2012).

Direct observations of the shape of halos is tricky, as there are only few tracers which offer a clear view on the vertical potential of the halo. The flat rotation curves of galaxies, while an excellent tracer of the radial potential of the halo, provides no information in the vertical direction. Luckily, some tracers do exist. The stellar streams of stripped, in-falling galaxies can be used to measure the potential the stream is traversing. Helmi (2004) analyzed the stream of Sagittarius, as found in the

2MASS survey, around the galaxy and found that the data best fits a model with a prolate shape, with an axis ratio of 5/3. In a similar fashion, only further out, do the satellites of the Galaxy offer such a tracer. Globular cluster NGC 5466 was modeled by Lux et al. (2012) and found to favor an oblate or tri-axial halo, while excluding spherical and prolate halos with a high confidence.

Gravitational lensing offers another measure of the vertical potential. Strong lensing uses the Einstein lens of background sources around a single galaxy / cluster. By modeling the lens, it is possible to create a detailed mass map of the system. By combining this with gas and stellar kinematics, it is possible to calculate the dark matter mass distribution (Treu 2010). For example, Barnabè et al. (2012) applied this method to lensed galaxy SDSS J2141, to find a slightly oblate halo ($q = 0.91_{-0.13}^{+0.15}$).

Weak lensing lacks the clear gravitation lens seen in strong lensing. As such it is unable to measure the halo of a single galaxy. Instead it provides an average halo shape from a statistically large sample of sources, by modeling the alignment of the background galaxies to a large series of foreground galaxies. This allows the sources to probe the outer edges of halos. A recent analysis by van Uitert et al. (2012) finds, on a sample of 2.2×10^7 galaxies, that the halo ellipticity distribution favors oblate, with $q = 0.62_{-0.26}^{+0.25}$.

Another way to place constraints on the halo shape is by carefully modeling local edge-on galaxies. The thickness of the HI layer in spiral galaxies depends directly on the local hydrostatic equilibrium. The HI layer flares strongly at large radii, as there is less matter gravitationally binding it to the central plane. Because of this, flaring provides a sensitive tracer of the vertical potential as function of radius in the disk. By combining this with the horizontal potential as gained from the rotation curve, and estimates for the gas and stellar mass distributions, one can fit the potential well created by the dark matter halo. This method was first applied to the Galaxy by Celnik et al. (1979). van der Kruit (1981) applied the method to edge-on galaxy NGC 891, finding that the halo was not as flattened as the stellar disk. NGC 4244 was analyzed by Olling (1995), who found a highly flattened halo of $q = 0.2_{-0.1}^{+0.3}$. Banerjee et al. (2010) analyzed UGC 7321 and found a spherical halo. These authors assumed a constant velocity dispersion, or at max a decreasing gradient, in their work. O'Brien et al. (2010d) set out to also measure the velocity dispersion as function of radius. Using that approach to measure the halo shape of UGC 7321, they find a spherical halo ($q = 1.0 \pm 0.1$).

For a more extended introduction on the history of the dark matter problem, we refer the reader to van der Kruit & Freeman (2011) and Sanders (2010).

In this series of papers, we will continue the work started by O'Brien et al. (2010b,c,d,a), which aims to use the rotation curve and flaring to derive the shape of dark matter halos in which the galaxies are embedded. In this first paper, we present our sample of 8 nearby, edge-on galaxies and their HI properties. Since O'Brien et al. (2010a), many of these galaxies have been re-observed by various groups, and we include these observations for a significant improvement. In paper II we present our new HI fitting tool GALACTUS, which will be applied to the cubes in paper III. In paper IV we present and model the stellar mass distributions based on optical and near-infrared

Table 1: General properties of the galaxies in this survey.

Distances are based on the Tully-Fisher relationship (TF) or the tip of the Red Giant Branch (TRGB). References: (1): This work, (2a): (Tully et al. 2008), (2b): (Radburn-Smith et al. 2011), (2c): (Matthews 2000), (3): (de Vaucouleurs et al. 1991), (4a): (Skrutskie et al. 2003) or (4b): (Jarrett et al. 2003)

Galaxy	RA	DEC	PA	Dist		Scale pc/arcsec	Morphology	H_{tot} (mag)
	(1)	(1)	($^{\circ}$) (1)	(Mpc) (2)	(2)			
IC 2531	9:59:55.5	-29:37:01.9	15.3	27.2	TF (a)	131.7	Sc	8.835 (b)
IC 5052	20:52:05.3	-69:12:04.2	128.2	5.7	TRGB (b)	27.4	SBd	9.102 (b)
IC 5249	22:47:06.0	-64:50:02.7	75.5	32.1	TF (a)	155.4	SBd	12.314 (a)
ESO 115-G021	2:37:47.2	-61:20:12.7	226.8	4.9	TRGB (a)	23.8	SBdm	14.301 (a)
ESO 138-G014	17:07:01.4	-62:05:14.3	314.6	15.8	TF (a)	76.5	SB(s)d	10.663 (b)
ESO 146-G014	22:12:59.8	-62:04:06.9	222.8	21.7	TF (a)	105.1	SBd	-
ESO 274-G001	15:14:14.6	-46:48:21.6	232.7	3.0	TRGB (a)	14.6	SAd	8.416 (b)
UGC 7321	12:17:34.4	+22:32:25.9	8.2	10.0	TRGB (c)	48.5	Sd	10.883 (b)

imaging. Paper V will then present the derived dark matter halo shapes.

This paper follows the following outline. In section 2 the criteria which define our sample are outlined, as well as the origin of the observations. Section 3 details how the data has been reduced. The results are then presented in section 4, followed by a discussion in section 5. For ease of comparison between figures, we have opted to present the main figures at the end of the paper.

2. Sample & Observations

Our sample is the same as that of O’Brien et al. (2010a). Criteria for the galaxies were that they lie in the southern sky, close to edge-on ($a/b \geq 10$), avoiding Galactic latitudes $||b|| \leq 10^{\circ}$ as to avoid optical and infrared extinction, relatively bulge-less (Hubble type Scd-Sd), nearby to be able to resolve the flare ($d \leq 30$ Mpc) and with a minimal integrated flux of 15 Jy km s^{-1} . This led to a sample of 5 edge-on galaxies. Several other galaxies were added for various reasons. UGC 7321 was added due to the availability of very good archival data, from the work by Uson & Matthews (2003). ESO 274-G001, despite its low Galactic latitude of 9.3° , was included for its exceptional proximity. IC 2531, a box/peanut bulge, barred galaxy, was included as a test of halo shapes under different types of mass scales and stages of secular evolution. We list the global properties of the sample in table 1. We also present the sample in the optical in figure 1.

The observations presented here come from both archived data as well as new observations. Almost all were observed using the Australian Telescope Compact Array (ATCA) near Narrabri, Australia. The only exception is UGC 7321, which was based on archived observations from the Very Large Array (VLA). O’Brien et al. (2010a) also included ATCA observations for this galaxy, but we found that this limited 4 hour observation reduced the quality of the data. Most of the observations came from previous archived observations by various authors over a span of years, going all the way to 1993. A significant number of these observations was already used by O’Brien et al. (2010a). A major new set of observations came as part of the work undertaken by the The Local Volume HI Survey (LVHIS) (Koribalski 2008). For ESO 138-G014 and ESO 274-G001 we have taken new observations using the ATCA. The various observations and configurations are listed in table 4.

3. Reductions

3.1. Calibration & Imaging

The calibration and imaging of the data has been done in MIRIAD (Sault et al. 1995). All subsequent analysis was done in PYTHON. All archived data from the ATCA was taken in the XX and YY polarizations. The new observations also include the XY and YX polarizations. We made use of the pre-calibrated UV data from O’Brien et al. (2010a), although we have re-reduced parts where we believed improvements could be made.

The data was first imported and split into the various observations, excluding any telescope shadowing. We then inspected all data for RFI and flagged where necessary. The primary and secondary calibrator were then used to calculate the gains and bandpasses. This was then applied to the main target. The continuum was then subtracted from the UV data.

The imaging was done using a three pass strategy, similar to O’Brien et al. (2010a). Since some of the data has pointing offsets for the same galaxy, we used the MIRIAD “joint approach” to invert the data in mosaic mode. The data was imaged in Stokes II, which is a special case of Stokes I, under the assumption of an unpolarized source. A robust parameter of 0.4 was used to provide a good balance between beamsize and sidelobes.

In the first pass we cleaned the full cube, using the `mosdmr` task. This was then restored, which resulted in an estimate for the major and minor axis of the beam. This was taken as the basis for the second pass. Here we used a square cell-size of one third of the major axis of the beamshape. The central quadrant was again cleaned and restored, using a circular beam with the major axis beamshape from the previous pass. The restored cube was smoothed to twice the beamsize and the RMS noise determined. We defined a regions mask in the cube where the signal was double the RMS. This was used in the third pass to perform a deep-clean on the data, where we cleaned the data to a cut-off level of half the RMS noise. The final cube was then restored.

We also produced low resolution cubes with a beam of $30''$ to search for any faint, extended component. This was done by tapering the invert to $30''$. The clean was then based on the same regions as the high resolution cube. In some cases we found the regions to be too tight for the low resolution beam. The regions were then broadened and both the high- and low-resolution cubes were again cleaned and restored using these wider regions.

Table 2: Global properties of the HI cubes.

Galaxy	High Resolution					Low Resolution				
	θ_{FWHM} (arcsec)	Δv (km/s)	σ ($\frac{\text{mJy}}{\text{beam}}$)	σ (K)	σ atoms/cm ²	θ_{B} (arcsec)	Δv (km/s)	σ ($\frac{\text{mJy}}{\text{beam}}$)	σ (K)	σ atoms/cm ²
IC 2531	11.0	3.3	1.3	6.6	3.9×10^{19}	30.0	3.3	1.9	1.3	7.8×10^{18}
IC 5052	11.0	3.3	1.1	5.6	3.4×10^{19}	30.0	3.3	1.6	1.1	6.4×10^{18}
IC 5249	8.2	3.3	1.4	12.3	7.4×10^{19}	30.0	3.3	2.5	1.7	9.9×10^{18}
ESO 115-G021	10.6	3.3	0.9	4.9	3.0×10^{19}	30.0	3.3	1.4	0.9	5.4×10^{18}
ESO 138-G014	10.8	3.3	2.2	11.3	6.8×10^{19}	30.0	3.3	3.1	2.1	1.3×10^{19}
ESO 146-G014	9.8	3.3	1.2	7.4	4.4×10^{19}	30.0	3.3	1.8	1.2	7.3×10^{18}
ESO 274-G001	12.2	3.3	1.3	5.1	3.1×10^{19}	30.0	3.3	1.7	1.2	7.0×10^{18}
UGC 7321	13.8	5.2	0.3	1.1	9.9×10^{18}	30.0	5.2	0.5	0.4	3.5×10^{18}

The VLA data for UGC 7321 consisted of very small band-passes, such that there was no possibility to perform a continuum subtraction in the UV. The continuum was therefore subtracted in the image plane. The above strategy led to a beam of 15 arcsec for UGC 7321. We have applied an additional sidelobe suppression of 700 arcsec to the beam, which led to the smaller beam as reported here.

3.2. Analysis

The noise in a mosaicked cube varies with position. It is therefore important to measure the noise close to the galaxy, while avoiding any contamination from the galaxy. The regions mask offered a good tool for this. We created a zeroth order moment map from these regions, which defined the maximum extent of the galaxy. The noise was then measured on the pixels in every channel that were inside this moment zero map, but were outside the specific region in that channel. We show the noise estimates in table 2. We convert from intensity I in Jy/beam to surface brightness temperature T_B in Kelvin, and to column densities n_{HI} in atoms/cm², using equations 1 and 2.

$$T_B = 606000 I / \theta^2 \quad (1)$$

$$n_{\text{HI}} = 1.8127 \times 10^{18} T_B \Delta v \quad (2)$$

The central position and position angle (PA) were derived from the high resolution cubes. First the cube was clipped below 30K, as the lower intensity regions were often found to be asymmetrical. A clear example of this asymmetry can be seen in IC 5052 (see figure 5c). We then created a moment zero image of the cube. The center of the galaxy was found as the minimal χ^2 of the difference between the image and its 180° rotated counterpart, as trialled over a wide range of positions. The position angle was then found by rotating the galaxy over a range of possible angles around this central position. The lowest χ^2 between the rotated images and its upside-down flipped counterpart gave the position angle. We set all position angles such that the approaching side will align with the left-hand side of the position-velocity diagram. The results for this are accurate to within 0.1 pixel and 0.1 degree and are listed in table 1.

Both the high and low resolution cubes were rotated, using the central position and PA, such that the major axis of the galaxy was aligned with the horizontal. We created zeroth moment maps for both rotated cubes, again with two times the RMS noise clipping. These cubes are shown in *c* parts of figures

1-8. The high resolution zeroth moment map was also used to created contour levels on top of the Digital Sky Survey (DSS) J-band image for that region. These are shown in the *a* parts of figures 1-8.

It was also interesting to see the maximum brightness temperature maps of the galaxies, as these would be instrumental in detecting any potential optical depth issues. The cube was converted from intensities I in mJy/beam to brightness temperatures T_B in K, using equation 1. We created a maximum brightness temperature map by selecting the maximum temperature along the velocity axis v for each position r, z . These are shown in the top plot of the *b* parts of figures 1-8. The middle plot shows the maximum temperature along the minor axis z for each position r, v . This creates an equivalent to a position-velocity diagram, only here it shows the maximum temperature regardless of height z . The lower plot takes the maximum brightness temperature along both v and z , and infers the corresponding optical depth, based on a assumed spin temperature of 125 K. We chose the values to lie close to the mean observed values for the cold neutral medium (CNM) (Dickey et al. 2009). As such it forms a diagnostic tool for potential self-absorption issues. We calculated the opacity τ using equation 3

$$\tau = -\log(1 - T_B/T_s) \quad (3)$$

The integrated position-velocity (PV) diagrams are shown in the *d* parts of figures 1-8. These have been created by integrating the rotated high-resolution cubes along their minor axis and converting them to brightness temperatures. The right-hand panels show the integrated spectra $S(v)$, which were created by integrating the PV diagrams over the major axis. Similarly, we show the brightness per position in the lower plots, by integrating the PV diagrams over v .

The width of the profile at the 20% and 50% maximum intensity levels, W_{20} and W_{50} , were measured directly from $S(v)$. These were based on the low-resolution cubes, which were masked using the regions files. The integrated flux FI was also measured in this cube. We make no use of clipping, in contrast to O'Brien et al. (2010a). The total HI mass, M_{HI} , was derived using

$$M_{\text{HI}} = 2.36 \cdot 10^5 \times D^2 \times FI \quad (4)$$

where the adopted distance D is in Mpc as shown in table 1. The derived values for FI , M_{HI} , W_{20} and W_{50} are shown in table 3.

The systematic velocity v_{sys} was measured from the PV diagram in a method similar to the position finding. For a wide

Table 3: Spectral properties of the galaxies

Galaxy	v_{sys} (km/s)	v_{max} (km/s)	W_{20} (km/s)	W_{50} (km/s)	FI (Jy km/s)	M_{HI} (M_{\odot})
IC 2531	2463.8	260.5	484.8	468.3	41.7	$7.3 \times 10^{9.0}$
IC 5052	596.7	114.4	197.9	181.4	117.7	8.9×10^8
IC 5249	2351.7	131.9	234.2	217.7	23.2	5.6×10^9
ESO 115-G021	514.2	85.1	141.8	125.3	109.0	6.2×10^8
ESO 138-G014	1492.3	130.9	237.5	227.6	48.9	2.9×10^9
ESO 146-G014	1678.8	84.1	148.4	128.6	17.5	1.9×10^9
ESO 274-G001	523.6	103.9	181.4	168.2	150.1	3.2×10^8
UGC 7321	409.3	128.8	237.0	221.6	41.7	9.8×10^8

range of possible systemic velocities v_{sys} , the PV diagram was rotated 180° around that velocity. The rotated PV-diagram was subtracted from the original, with the lowest χ^2 giving v_{sys} . The maximum velocity v_{max} was calculated by finding the furthest channel from v_{sys} that still contained flux above two times the RMS noise level. The results for v_{sys} and v_{max} are also shown in table 3. We have also prepared a document with all our channel-maps, which is available on request.

4. Results

4.1. IC 2531

Galaxy IC 2531 is the only Sc galaxy in our sample. The classification is different from that of Bureau & Freeman (1999) and O’Brien et al. (2010a), where the galaxy has been classified as an Sb galaxy. As an Sc galaxy, it has the largest gas mass of the sample, and has a maximum rotation velocity v_{max} which is twice as high as the rest of the sample (table 3). The HI layer is remarkably flat, with the disk seemingly having a smaller scale-height than the stellar disk (figure 4a).

Based on the double horns in the integrated profile, we would expect the galaxy to be fairly symmetric (figure 4d). The PV diagram itself is, however, fairly asymmetric. Interestingly, HIPASS also reports a more asymmetric profile. The asymmetry is also present in the analysis of the galaxy in O’Brien et al. (2010c, figure 15), where the two sides of the derived surface density can be seen to deviate strongly.

The PV-diagram shows a so-called “figure 8”-pattern, for which Bureau & Freeman (1997) suggest that it is due to a very extended weak bar. This bar did not show up in the $H\alpha$ analysis of Bureau & Freeman (1999), although they suffered from background problems for this galaxy. This was not fully unexpected, as Bureau & Freeman (1997) already noted that the figure extended over a very long range. They speculated that the figure might also be due to a warp, density ring or a spiral arm. Ann & Park (2006) reported that there is indeed a warp in this galaxy. We also believe it more likely that this pattern is associated with the warp and does not represent a bar. The warp is visible in figure 4c.

The PV-diagram is also asymmetric in the rotation curve. The receding side shows a slowly increasing rotation curve, while the approaching side show a sharp increase followed by a flat rotation.

The maximum surface brightness temperature map (figure 4b) shows a strong central peak and some additional peaks. There does not appear to be symmetry in the distribution of these peaks. They are most likely due to local events in the gas, such as supernova or a burst of star formation.

4.2. IC 5052

IC 5052 is a nearby SBd galaxy. The bulge is clearly visible in figure. 5a. We find a previous unreported, line-of-sight warp in the outskirts of the galaxy. This is particularly clear in the zeroth moment map of the low resolution cube (figure 5c). Further modeling will be required to confirm this as a true warp. For now, we note that the channel maps are very similar to the fitted model of the line-of-sight warp in ESO 123-G13 (Gentile et al. 2003). The warp appears to be symmetric in pitch angle, although it is more extended towards the lower-left side. We have overlaid the contour-maps on top of various optical and infrared images that were available, but we can find no optical counterpart to the warp.

The PV diagram of this galaxy (figure 5d) shows signs of this warp beyond 250 arcseconds. The main part of the profile looks like a solid-body rotator. The high- and low velocity sides are asymmetric, which is also clear from the integrated profile. The shape of the spectrum does agree well with the profile from HIPASS.

The maximum surface brightness temperature profile of figure 5b shows a plateau around 80-100 K for most of the inner part of the galaxy. Only the central part shows a higher temperature, rising to a maximum of 140 K. This central over-density is also visible in the moment 0 maps (5c). O’Brien et al. (2010a) identify this as a star forming region.

4.3. IC 5249

IC 5249 is the most distant galaxy in our sample, at a distance of 32 Mpc. The galaxy is only 5 arcminutes. This is still enough to fully resolve the HI disk in both width and height. The maximum S/N of the cube has not been improved since O’Brien et al. (2010a), and is still around 10.

The maximum temperatures exhibit a plateau between 80-100 K, over the radius -100 and 100 arcseconds, most of the galaxy (figure 6b). Another plateau is visible in integrated flux along the major axis (6d), wherein over that same region the intensity is seen to hover around 0.06 Jy km/s / arcsec. The PV-diagram itself is slightly asymmetric, with the higher velocity side having more mass than the low velocity side.

van der Kruit et al. (2001) have previously analyzed the rotation curve of the galaxy, using HI and $H\alpha$. They find the galaxy to exhibit a steep rising rotation curve, where-after it flattens out to $v_{\text{max}} \approx 100$ km/s.

There is a faint indication of a warp, visible in the lower plot in figure 6c.

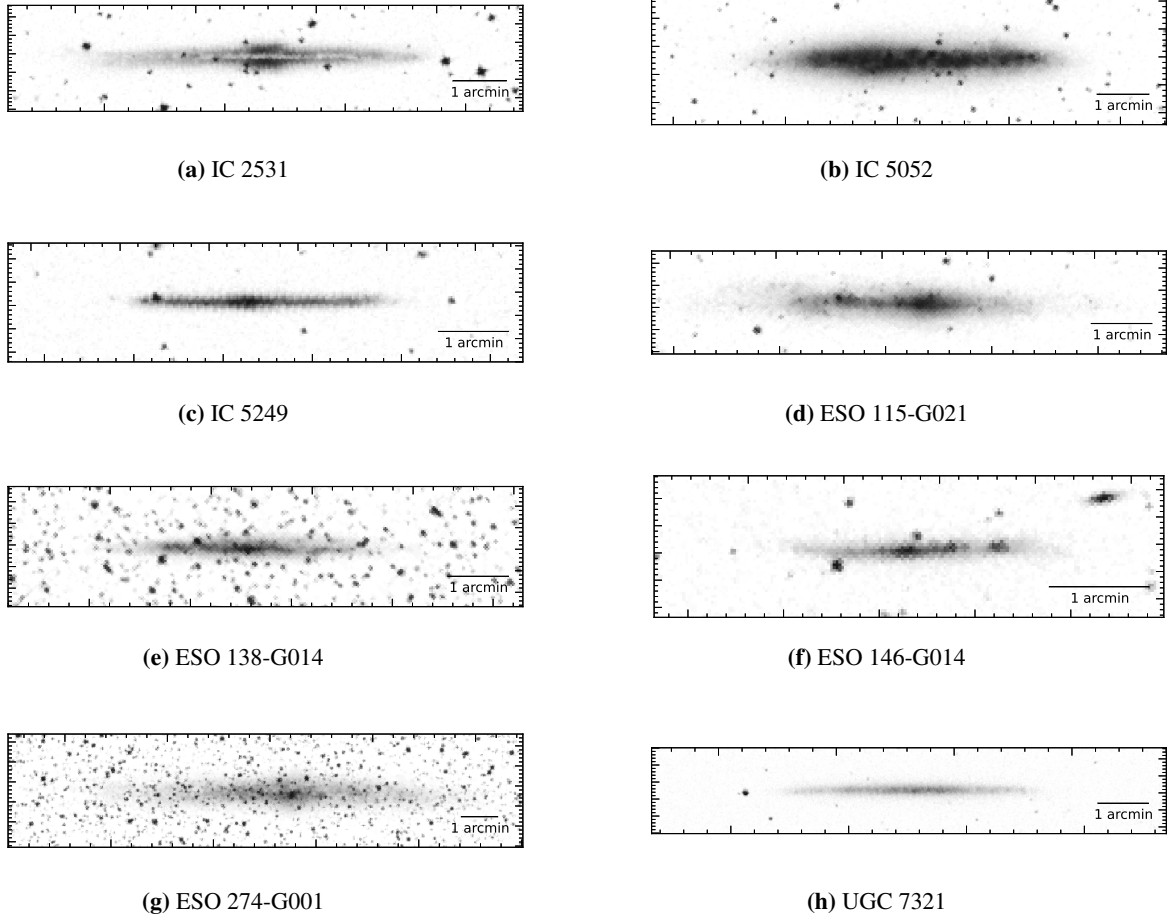


Fig. 1: Overview of the sample in the DSS J-band.

4.4. ESO 115-G021

ESO 115-G021 is a nearby SBdm galaxy at a distance of only 4.9 Mpc. A lot of data was available, totaling to 83.5 hours. Due to this, it is a very well resolved galaxy. The plane of the galaxy is over ~ 80 beams wide and the galaxy is ~ 10 beams in height (see figure 7a).

The derived spectrum is more symmetric than the HIPASS spectrum, which has a larger peak at the high-velocity side. There is a gas-cloud at 02:36:59 -61:18:41 visible in multiple channels. It is shown in both the high and low resolution cubes (figure 7c) at position (180", 300"). In the PV diagram (figure 7d) it is visible as the small upward peak between 500 and 515 km/s. This close proximity to the galaxy in both velocity and distance indicates the gas is associated with the galaxy. The cloud is invisible in the DSS, I and V bands paper IV, indicating that it has negligible stellar content. The gas cloud has a HI mass of $3.75 \times 10^5 M_{\odot}$.

The PV-diagram (figure 7d) shows an asymmetry, with the high velocity side being more extended than the low velocity side. This is most likely due to the warp, which is visible in the zeroth moment maps (figure 7c). The main component of the PV-diagram shows solid body rotation.

The maximum temperature map (figure 7b) shows that this warp has a surface brightness of 20-30 K. The more stable inner parts of the disk show a maximum temperature plateau around 80-90 K, with the strong exception of the region between 0" and

+50", where there is a rise to a maximum of 140 K. This region corresponds to a bright region of the DSS image, and is likely due to star formation.

4.5. ESO 138-G014

Galaxy ESO 138-G014 is the least observed galaxy in our sample. Nevertheless, the galaxy is well resolved by the telescope. The minor axis of the galaxy in particular is covered by roughly 6 beams.

The PV-diagram (8d) is asymmetric, with the receding side showing an extended component. This is associated with a warp, as visible in figure 8c. No optical counterpart to this warp is known (Sánchez-Saavedra et al. 2003).

The maximum brightness temperature map resembles a plateau for most of the galaxy, averaging between 80 and 100 K (figure 8b). The only exception is at the left side, where a peak of 140 K is attained. This corresponds to the bright region in the south-west region in the DSS image (figure 8a), and is most likely a star forming region.

4.6. ESO 146-G014

Galaxy ESO 146-G014 is the faintest galaxy in our sample. The moment zero maps (figure 9b) show that the galaxy does not appear to have a fixed plane. Instead it looks slightly bent. This

is most likely due a strong warp, which can also be seen in the visible in the DSS J-band image (figure 1f).

The PV diagram (figure 9d) looks symmetrical, although the integrated spectrum is more asymmetric than the HIPASS spectrum, with a stronger peak at the low-velocity side. Overall the galaxy appears to exhibit solid-body rotation.

The maximum surface brightness temperatures appear to form a plateau over major part of the galaxy, averaging around 90 K (figure 9b). On the left-hand side of the galaxy, this maximum drops relatively slowly towards the warp.

4.7. ESO 274-G001

ESO 274-G001 is an SAd galaxy. At only 3.02 Mpc, it is the closest galaxy in our sample. It is also has the least HI mass of the galaxies in our sample (table 3). Due to its proximity, it is still the largest galaxy in terms of angular size, spanning 13 arcminutes in width. In height it is also very well resolved, covering at least 80 arcseconds.

The central hole in the zeroth moment image (figure 10a) is an artifact, due to the removal of a continuum radio source at this coordinate. The most likely explanation is a active galactic nucleus (AGN). It is likely at the galactic center (see table 1) and we have therefore manually centered the galaxy on this position.

AGN are known to exert strong influence on the ISM of the galaxy (e.g. Shulevski et al. (2012) and references therein). It is therefore interesting to note how regular the HI disk is, both in the zeroth moment as in maximum temperature. Most of the inner disk shows a maximum surface density remarkably flat plateau between 80 and 100 K (figure 10b). The galaxy is barely visible in most optical and infrared bands, indicating only little stellar mass. This may explain why the gas relatively undisturbed, in comparison with our other galaxies.

There is a warp visible beyond ~ 280 arcsec on both sides of the galaxy (figure 10c). The PV-diagram is slightly asymmetric, with more gas at the low velocity side. This is also visible in the integrated profiles (figure 10d). The shape of the spectrum matches well to HIPASS, although it is more symmetric.

4.8. UGC 7321

UGC 7321 is a well known low surface brightness galaxy, which has already been studied using the Westerbork Synthesis Radio Telescope (WSRT) García-Ruiz et al. (2002) and the VLA Uson & Matthews (2003). The observations by Uson & Matthews (2003) form the basis of our work here. In terms of noise levels, it is the best resolved galaxy in our sample. It is also our only northern sky galaxy.

The zeroth moment map 11c shows a well behaved, symmetric galaxy. Only at the outskirts is there some indication of warping, a feature already noted by Matthews & Wood (2003), who also notes is flaring. Additionally, they find evidence that suggests the presence of a neutral gas halo. We believe that this halo might be visible as the extended structure on the lower figure, between 0 and 110 arcseconds.

The PV-diagram of the galaxy is asymmetric. The receding side looks more like a flat rotation curve than the approaching side, which continue to rise over much of the galaxy.

The maximum surface brightness map shows a clear central peak and two additional peaks around 100 arcseconds (figure 11b). These peaks appear to be symmetric around the center of the galaxy. The rest of the galaxy forms a plateau, around 60

K. We again see that the maximum temperature trails slowly off into the warp on the right-hand side.

5. Discussion

The spatial resolution of the high resolution cubes is on average 1-2" larger than O'Brien et al. (2010a) (table 2). This is due to most of the new observations being in tight configurations. There are therefore more short baselines. The weight in the UV-plane shifts to slightly smaller scales, resulting in larger beams. The effect is small enough to be of little importance to this work, as the vertical scale of the galaxies is still fully resolved.

In the high resolution cubes, the noise is significantly lower, thanks to the additional observations and larger beams. Where no additional observations were available, the noise is (as expected) roughly equal. The surprising differences is in the column density noise levels. It seems that O'Brien et al. (2010a) has not integrated the column densities over channel width. If this is taken into account, the values are again comparable.

Overall there is some disagreement with O'Brien et al. (2010a) on the derived central positions, mostly because we include more faint extended emission in our measurements. The biggest offset is in ESO 138-G014 (see figure 8c), where the non-symmetric warp is affecting the position estimate. The position angles however, do agree well. Similarly, the systemic velocities v_{sys} and associated parameters $W20$, $W50$ and v_{max} are all well determined. Kinematic modeling will have to be performed to find the true center of each galaxy, the derived values here will only serve as first estimates in paper III.

We have also compared the integrated flux FI with the HIPASS catalog (Doyle et al. 2005) and the work by O'Brien et al. (2010a). In general our results match well to HIPASS. ESO 274-G001 has the largest difference, with 25 mJy km/s more detected here than in HIPASS. The other major differences are for ESO 115-G021 with a difference of 19 mJy km/s, and IC 5052 with a difference of 7 mJy km/s. Both have again more flux in our work.

These three galaxies are the largest in the sample. The Parkes single dish beam has a angular resolution of 15.5 arcminutes. Most likely the Parkes beam fails to cover the entire galaxy, missing the outskirts and is therefore getting a lower total flux. With that variation in mind, each datacube has successfully recovered all flux from HIPASS.

O'Brien et al. (2010a) reports very different values for FI . Most striking is IC 5052, where only 37.9 mJy km/s is reported, against 117.7 mJy km/s here. It is unclear to us why O'Brien et al. (2010a) often reports very different values. Most likely it has to do with the masking of extended emission in their work.

As noted before, the distances to the galaxies are assumed further than in O'Brien et al. (2010a). That change plus the higher values for FI combine to have a large impact on the induced total mass M_{HI} of the galaxy. Most galaxies now have estimated masses anywhere between 20-300% more.

All eight of our galaxies shows signs of warping. This is consistent with the work by García-Ruiz et al. (2002), who found that all galaxies with extended HI disk have warps. All of

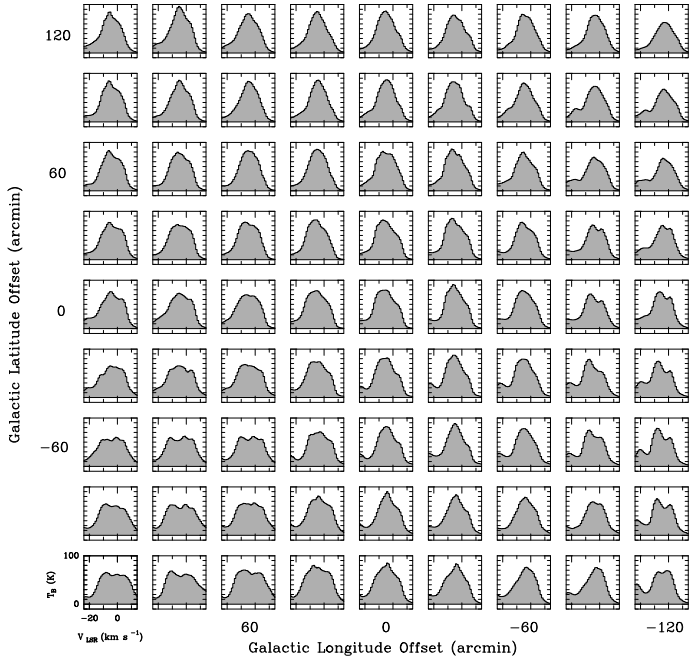


Fig. 2: Overview of a sample of Galactic HI clouds in a 4 X 4 degree patch of sky, as assembled by Allen et al. (2012, figure 3) from archival HI survey data. The various clouds exhibit a remarkably uniform behavior.

the warps occur at or just beyond the visible stellar disk, similar to the findings by van der Kruit (2007). The only possible exception to this rule could be ESO 146-G14, which seems to have the stellar disk embedded in the warp (see figure 9a) However, the overall HI layer appears to be bent in this galaxy, with the gas not following a single plane. It could therefore well be that we are dealing with a projection effect by the warp, where the true HI disk is still a single plane. Further modeling will be required before this can be confirmed.

5.1. The opacity of the HI layer

The 21-cm line of HI is known to be optically thick along many sight lines in our own (edge-on) Galaxy (Allen et al. 2012). Evidence is accumulating that flat-topped HI profiles characteristic of this effect are common in M31 and M33, where hydrogen mass correction factors of order 1.3 to 1.4 have been proposed (Braun 2012). Such self-absorption of the HI emission not only biases the total hydrogen masses, it also raises questions about the use of the HI velocity structure for studies of the gas kinematics. Nowhere are the answers to such questions more urgent than in the study of highly-inclined galaxies, where techniques have been proposed to “peel off” the edges of the observed HI in order to expose the detailed velocity dispersion of the ISM over large segments of the galaxy disks in both r and z (O’Brien et al. 2010b).

If a moderately inclined galaxy like M31 hides 34% of its HI mass (Braun 2012), what is the effect on edge-on galaxies? In the HI the dominating factor for self-absorption would be the spin temperature of the cold neutral medium, which would serve as an upper limit to the observable surface brightness temperature. Consider now the maximum surface brightness maps for ESO 274-G001 (figure 10b). There is a clear plateau

around 90 Kelvin throughout almost the entire galaxy. At the outskirts the line of sight is much shorter than near the inner parts, yet the observed peak temperature remains stable. As a case of even shorter path-lengths, consider Allen et al. (2012, figure 3) (reproduced here as figure 2), where a ‘mini-survey’ has been performed of HI, OH and CO at 30’ resolution inside the Galaxy. This gas is quite local, within about 2 kpc of the sun. Again we see a peak temperature of 90K, only this time in individual clouds. Why would such different path-lengths always result in the same brightness temperature?

The traditional view is that at these brightness temperatures, column densities are reached at which the atomic gas starts to be converted into molecular gas, thus providing a natural threshold to the observed temperatures (Stecher & Williams 1967; Hollenbach et al. 1971; Federman et al. 1979). A column density is however an artificial construct based on the position of the observer, and as such the gas cannot be expected to conform to it. A volume density threshold would seem to be a much more physically-relevant quantity. However, since the path-lengths between the local HI clouds from Allen et al. (2012) and the central parts of the edge-on galaxies presented here vary over roughly two orders of magnitude, the volume and the inferred density are also likely to vary in the same way. Any volume density threshold would seem to have difficulty explaining the close similarities in the maximum brightness temperatures.

Opacity however can explain this naturally. The brightness temperature of 90 Kelvin is in the same range as the expected spin temperature for the cold neutral medium (Dickey & Lockman 1990; Dickey et al. 2009). 90K is then the maximum ascertainable temperature before the gas turns optically thick. We are thus seeing optically thick gas in Allen et al. (2012). In figure 10b the path-lengths have become so long compared to the sizes of the clouds, that each line is bound to hit an optically thick cloud. Considering the radii at which these can be seen, a lot more than 30% of the galaxy HI mass could be hidden in and behind these clouds.

Another tempting argument in favor of this explanation comes from the study of local clouds in Allen et al. (2012, figure 5), reproduced here in figure 3. A remarkable linear relation is shown between the molecular OH (thermal 18cm emission) and HI surface brightnesses of the form $T_A(\text{OH}) \approx 1.50 \times 10^{-4} T_B(\text{HI})$. The OH and HI follow the same velocities and distributions. This relation holds for $T_B(\text{HI}) \leq 60\text{K}$. Beyond that the HI appears to saturate, leveling off completely around 90K. Yet the OH temperatures continues to rise. Could it be tracing a now-turned-opaque HI gas?

The lower panel in figures 4b to 10b show the inferred maximum self-absorption for a spin temperature of 125 K. A spin temperature of a 125 K is most likely an upper-limit for the CNM, yet it already implies a maximum opacity of $\tau \sim 1$. If true, this will have drastic implications for deriving the structure and kinematics, as traditional HI modeling tools work under the assumption of an optically thin gas. To deal with this, in our next paper we will present the new HI modeling and fitting tool GALACTUS, which can model self-absorption.

Acknowledgements. S.P. would like to thank Renzo Sancisi, Filippo Fraternali, Thijs van der Hulst, Marc Verheyen, Thomas Martinsson and Aleksander Schuvelski for useful debates, comments and suggestions. The Australia Telescope is funded by the Commonwealth of Australia for operation as

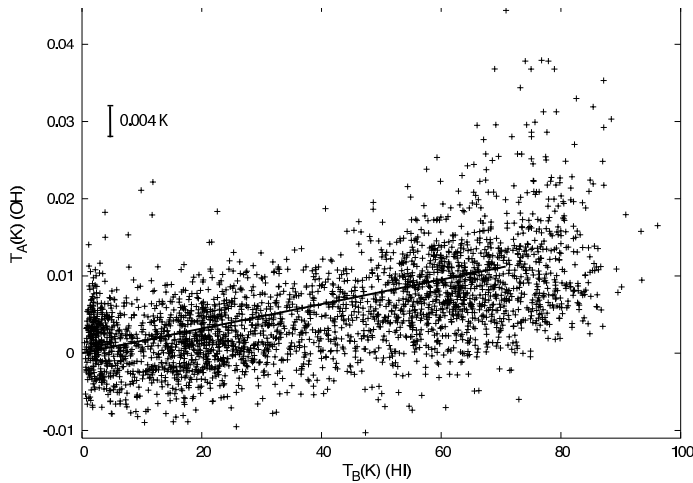


Fig. 3: The correlation between HI and OH surface brightness temperatures, reproduced from the Galactic mini-survey by Allen et al. (2012, figure 5). The HI and OH follow a linear correlation for most of the diagram. Beyond 90K the HI seems to saturate, while the OH continues to rise. Is the OH tracing an optically thick HI layer?

a National Facility managed by CSIRO. The National Radio Astronomy Observatory is a facility of the National Science Foundation operated under cooperative agreement by Associated Universities, Inc. The Digitized Sky Surveys were produced at the Space Telescope Science Institute under U.S. Government grant NAG W-2166. The images of these surveys are based on photographic data obtained using the Oschin Schmidt Telescope on Palomar Mountain and the UK Schmidt Telescope. The plates were processed into the present compressed digital form with the permission of these institutions. `PFITS` and `PYRAF` are products of the Space Telescope Science Institute, which is operated by AURA for NASA. This research has made use of the NASA/IPAC Extragalactic Database (NED) which is operated by the Jet Propulsion Laboratory, California Institute of Technology, under contract with the National Aeronautics and Space Administration. This research has made use of NASA's Astrophysics Data System.

References

- Allen, R. J., Ivette Rodríguez, M., Black, J. H., & Booth, R. S. 2012, *AJ*, 143, 97
 Ann, H. B. & Park, J.-C. 2006, *New A*, 11, 293
 Banerjee, A., Matthews, L. D., & Jog, C. J. 2010, *New A*, 15, 89
 Barnabè, M., Dutton, A. A., Marshall, P. J., et al. 2012, *MNRAS*, 423, 1073
 Bennett, C. L., Larson, D., Weiland, J. L., et al. 2012, *ArXiv e-prints*
 Bosma, A. 1981, *AJ*, 86, 1825
 Braun, R. 2012, *ArXiv e-prints*
 Bureau, M. & Freeman, K. C. 1997, *PASA*, 14, 146
 Bureau, M. & Freeman, K. C. 1999, *AJ*, 118, 126
 Celnik, W., Rohlfs, K., & Braunsfurth, E. 1979, *A&A*, 76, 24
 Davis, M., Efstathiou, G., Frenk, C. S., & White, S. D. M. 1985, *ApJ*, 292, 371
 de Vaucouleurs, G., de Vaucouleurs, A., Corwin, Jr., H. G., et al. 1991, *Third Reference Catalogue of Bright Galaxies*
 Dickey, J. M. & Lockman, F. J. 1990, *ARA&A*, 28, 215
 Dickey, J. M., Strasser, S., Gaensler, B. M., et al. 2009, *ApJ*, 693, 1250
 Doyle, M. T., Drinkwater, M. J., Rohde, D. J., et al. 2005, *MNRAS*, 361, 34
 Famaey, B. & McGaugh, S. S. 2012, *Living Reviews in Relativity*, 15, 10
 Federman, S. R., Glassgold, A. E., & Kwan, J. 1979, *ApJ*, 227, 466
 Freeman, K. C. 1970, *ApJ*, 160, 811
 Freese, K., Lisanti, M., & Savage, C. 2012, *ArXiv e-prints*
 García-Ruiz, I., Sancisi, R., & Kuijken, K. 2002, *A&A*, 394, 769
 Gentile, G., Fraternali, F., Klein, U., & Salucci, P. 2003, *A&A*, 405, 969
 Helmi, A. 2004, *ApJ*, 610, L97
 Hollenbach, D. J., Werner, M. W., & Salpeter, E. E. 1971, *ApJ*, 163, 165
 Jarrett, T. H., Chester, T., Cutri, R., Schneider, S. E., & Huchra, J. P. 2003, *AJ*, 125, 525
 José, J. & Iliadis, C. 2011, *Reports on Progress in Physics*, 74, 096901
 Karachentsev, I. D. 1966, *Astrophysics*, 2, 39
 Koribalski, B. S. 2008, *The Local Volume HI Survey (LVHIS)*, ed. Koribalski, B. S. & Jerjen, H., 41

- Lux, H., Read, J. I., Lake, G., & Johnston, K. V. 2012, *MNRAS*, 424, L16
 Matthews, L. D. 2000, *The Astronomical Journal*, 120, 1764
 Matthews, L. D. & Wood, K. 2003, *ApJ*, 593, 721
 McDonald, P., Seljak, U., Burles, S., et al. 2006, *ApJS*, 163, 80
 Milgrom, M. 1983, *ApJ*, 270, 365
 Monnier, J. D. & Allen, R. J. 2012, *ArXiv e-prints*
 O'Brien, J. C., Freeman, K. C., & van der Kruit, P. C. 2010b, *A&A*, 515, A61
 O'Brien, J. C., Freeman, K. C., & van der Kruit, P. C. 2010c, *A&A*, 515, A62
 O'Brien, J. C., Freeman, K. C., & van der Kruit, P. C. 2010d, *A&A*, 515, A63
 O'Brien, J. C., Freeman, K. C., van der Kruit, P. C., & Bosma, A. 2010a, *A&A*, 515, A60
 Olling, R. P. 1995, *AJ*, 110, 591
 Oort, J. H. 1932, *Bull. Astron. Inst. Netherlands*, 6, 249
 Ostriker, J. P. & Peebles, P. J. E. 1973, *ApJ*, 186, 467
 Raddburn-Smith, D. J., de Jong, R. S., Seth, A. C., et al. 2011, *ApJS*, 195, 18
 Roberts, M. S. & Whitehurst, R. N. 1975, *ApJ*, 201, 327
 Rogstad, D. H. & Shostak, G. S. 1972, *ApJ*, 176, 315
 Rubin, V. C. & Ford, Jr., W. K. 1970, *ApJ*, 159, 379
 Sánchez, A. G., Baugh, C. M., Percival, W. J., et al. 2006, *MNRAS*, 366, 189
 Sánchez-Saavedra, M. L., Battaner, E., Guíjarro, A., López-Corredoira, M., & Castro-Rodríguez, N. 2003, *A&A*, 399, 457
 Sanders, R. H. 2010, *The Dark Matter Problem: A Historical Perspective*
 Sault, R. J., Teuben, P. J., & Wright, M. C. H. 1995, in *Astronomical Society of the Pacific Conference Series*, Vol. 77, *Astronomical Data Analysis Software and Systems IV*, 433
 Schneider, M. D., Frenk, C. S., & Cole, S. 2012, *J. Cosmology Astropart. Phys.*, 5, 30
 Shulevski, A., Morganti, R., Oosterloo, T., & Struve, C. 2012, *A&A*, 545, A91
 Skrutskie, M. F., Cutri, R. M., Stiening, R., et al. 2003, *VizieR Online Data Catalog*, 7233, 0
 Stecher, T. P. & Williams, D. A. 1967, *ApJ*, 149, L29
 Steigman, G. & Turner, M. S. 1985, *Nuclear Physics B*, 253, 375
 Treu, T. 2010, *ARA&A*, 48, 87
 Tully, R. B., Shaya, E. J., Karachentsev, I. D., et al. 2008, *ApJ*, 676, 184
 Uson, J. M. & Matthews, L. D. 2003, *AJ*, 125, 2455
 van der Kruit, P. C. 1981, *A&A*, 99, 298
 van der Kruit, P. C. 2007, *A&A*, 466, 883
 van der Kruit, P. C. & Freeman, K. C. 2011, *ARA&A*, 49, 301
 van der Kruit, P. C., Jiménez-Vicente, J., Kregel, M., & Freeman, K. C. 2001, *A&A*, 379, 374
 van Uitert, E., Hoekstra, H., Schrabback, T., et al. 2012, *A&A*, 545, A71
 Vera-Ciro, C. 2013, *PhD thesis*, Kapteyn Astronomical Institute, University of Groningen
 Yang, J., Turner, M. S., Schramm, D. N., Steigman, G., & Olive, K. A. 1984, *ApJ*, 281, 493
 Zwicky, F. 1933, *Helvetica Physica Acta*, 6, 110

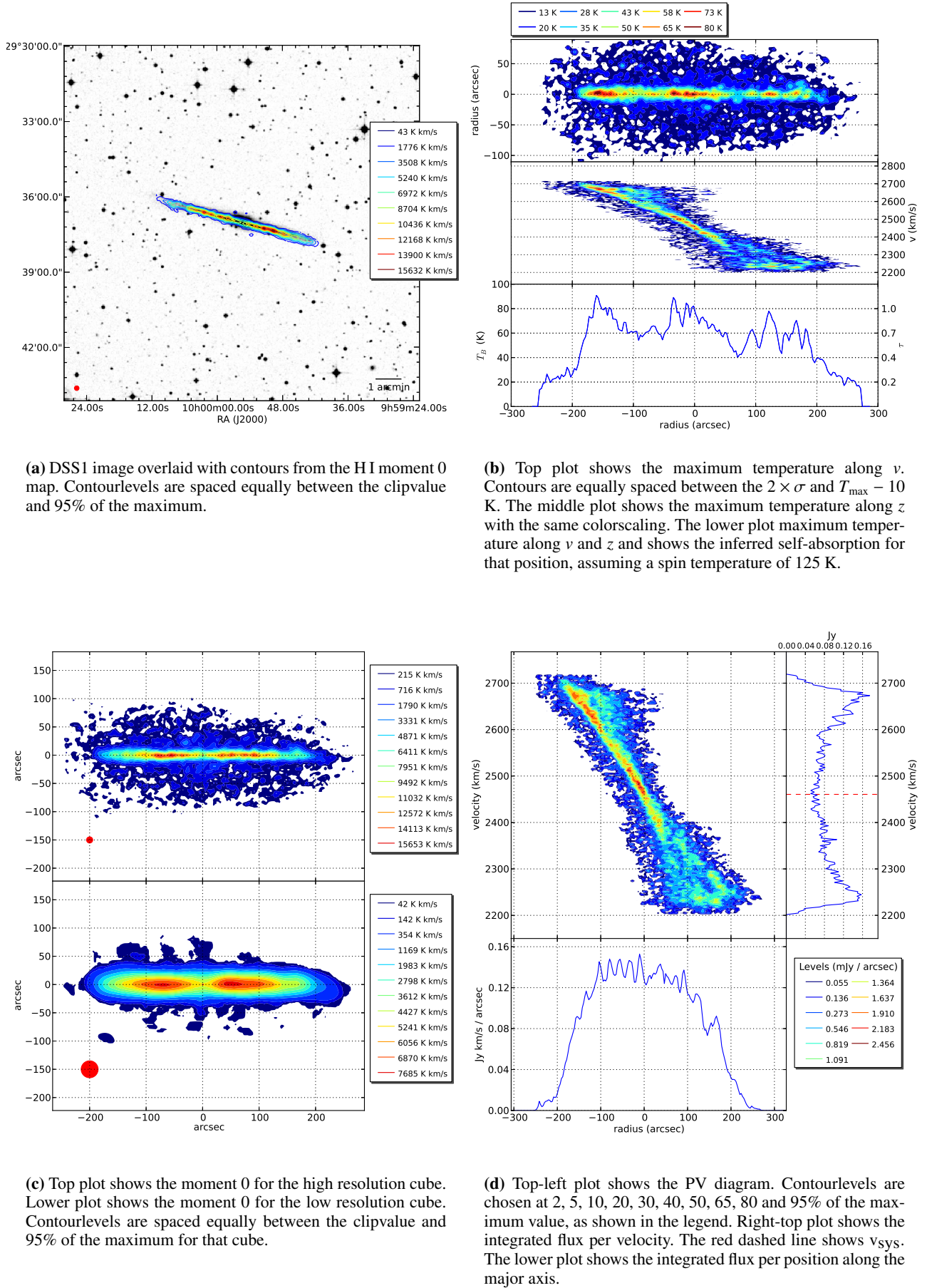


Fig. 4: Results for IC 2531

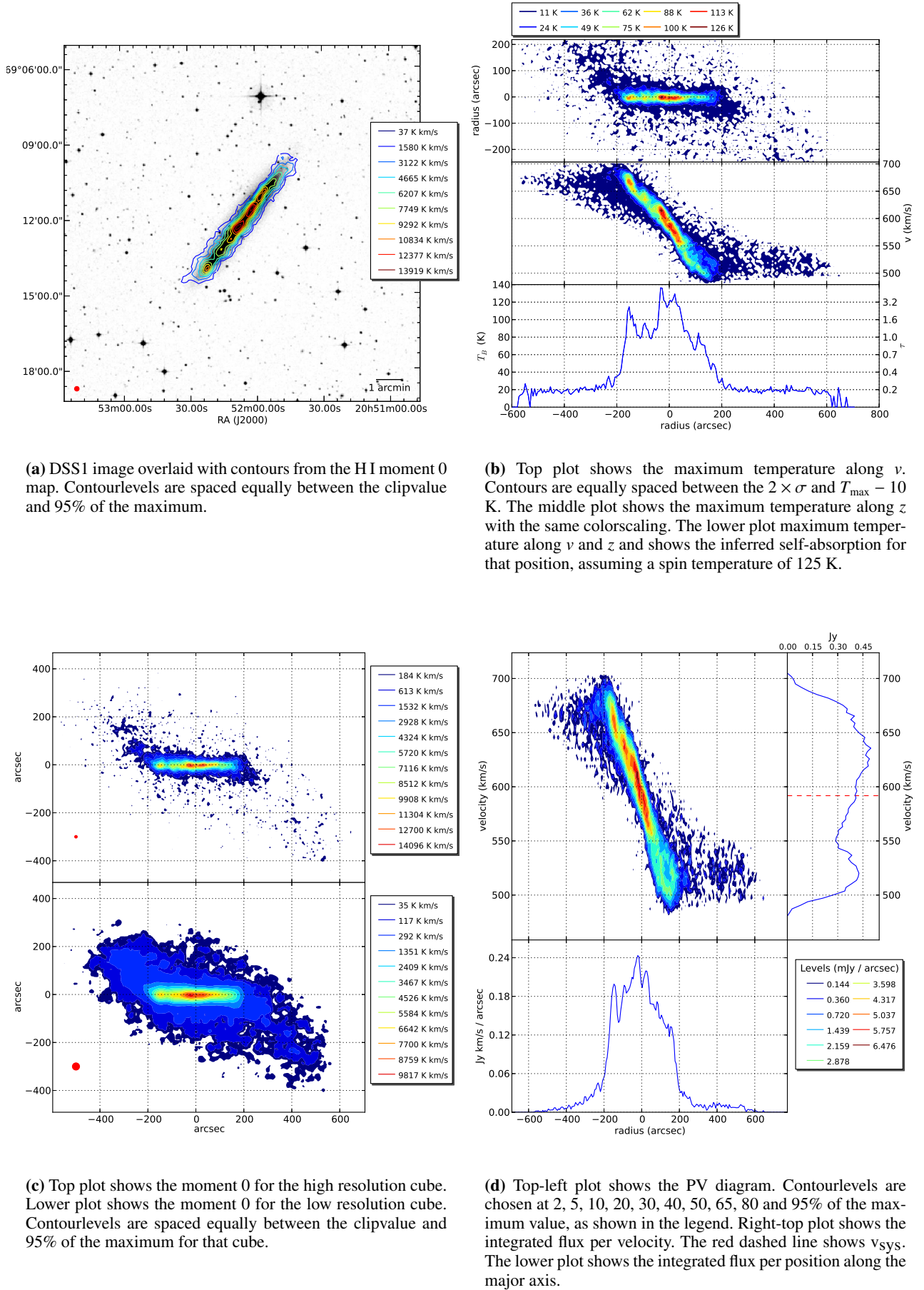
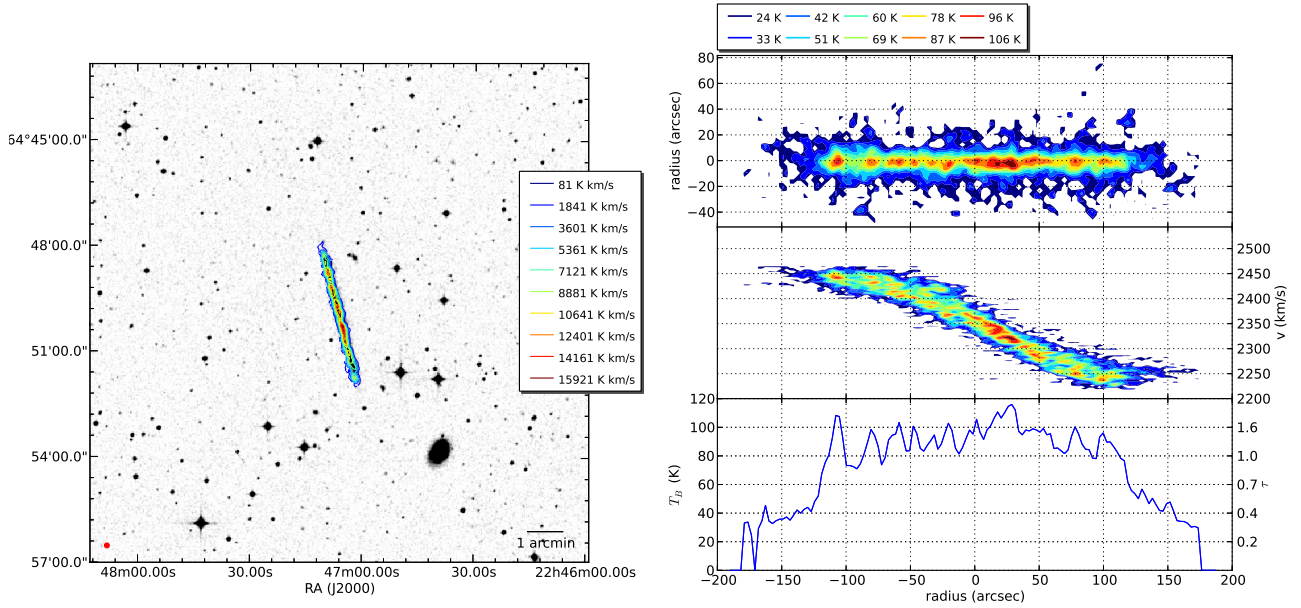
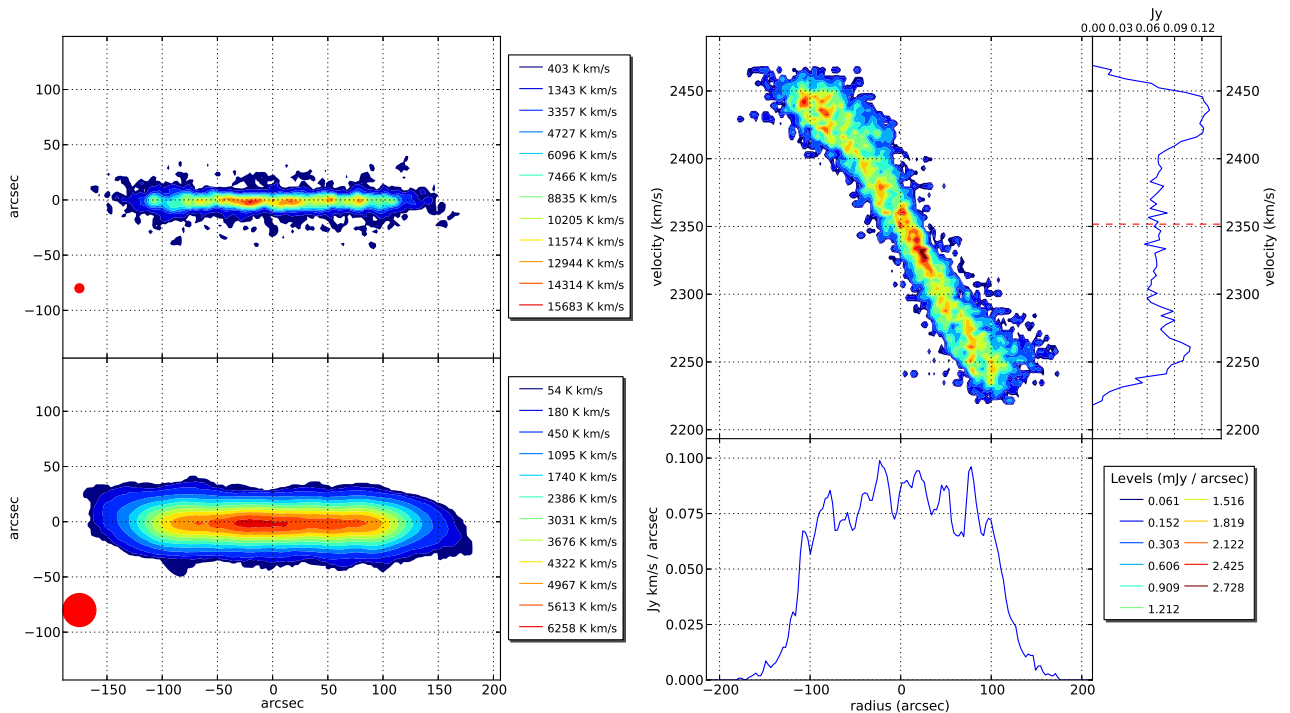


Fig. 5: Results for IC 5052



(a) DSS1 image overlaid with contours from the HI moment 0 map. Contour levels are spaced equally between the clipvalue and 95% of the maximum.

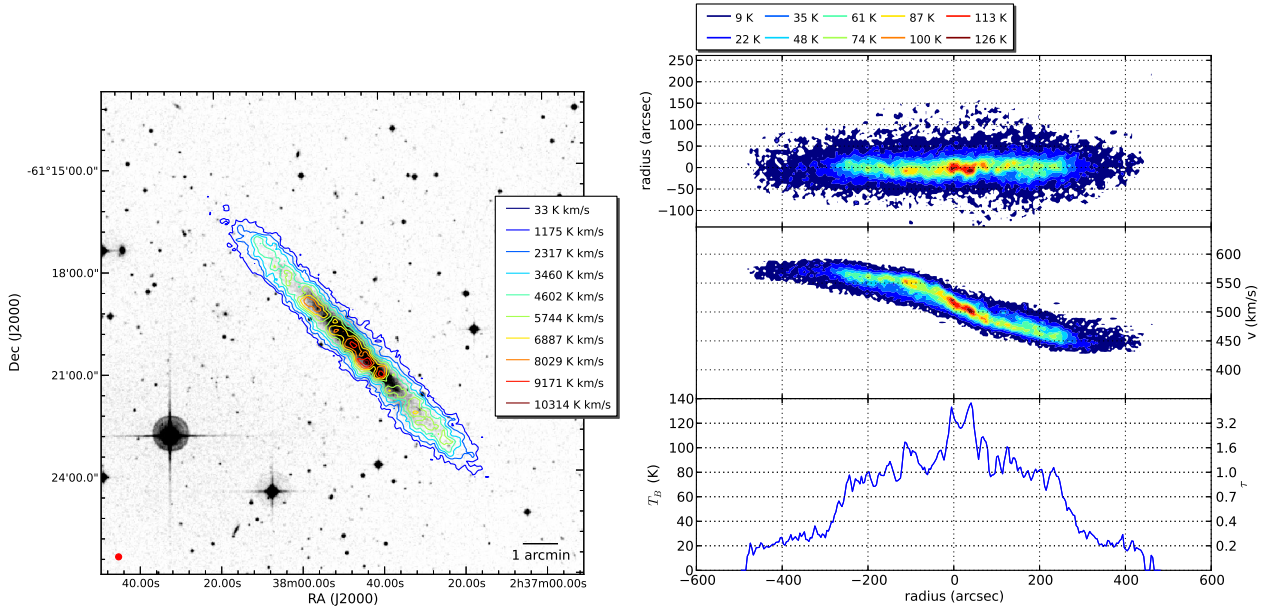
(b) Top plot shows the maximum temperature along v . Contours are equally spaced between the $2 \times \sigma$ and $T_{\max} - 10$ K. The middle plot shows the maximum temperature along z with the same color scaling. The lower plot maximum temperature along v and z and shows the inferred self-absorption for that position, assuming a spin temperature of 125 K.



(c) Top plot shows the moment 0 for the high resolution cube. Lower plot shows the moment 0 for the low resolution cube. Contour levels are spaced equally between the clipvalue and 95% of the maximum for that cube.

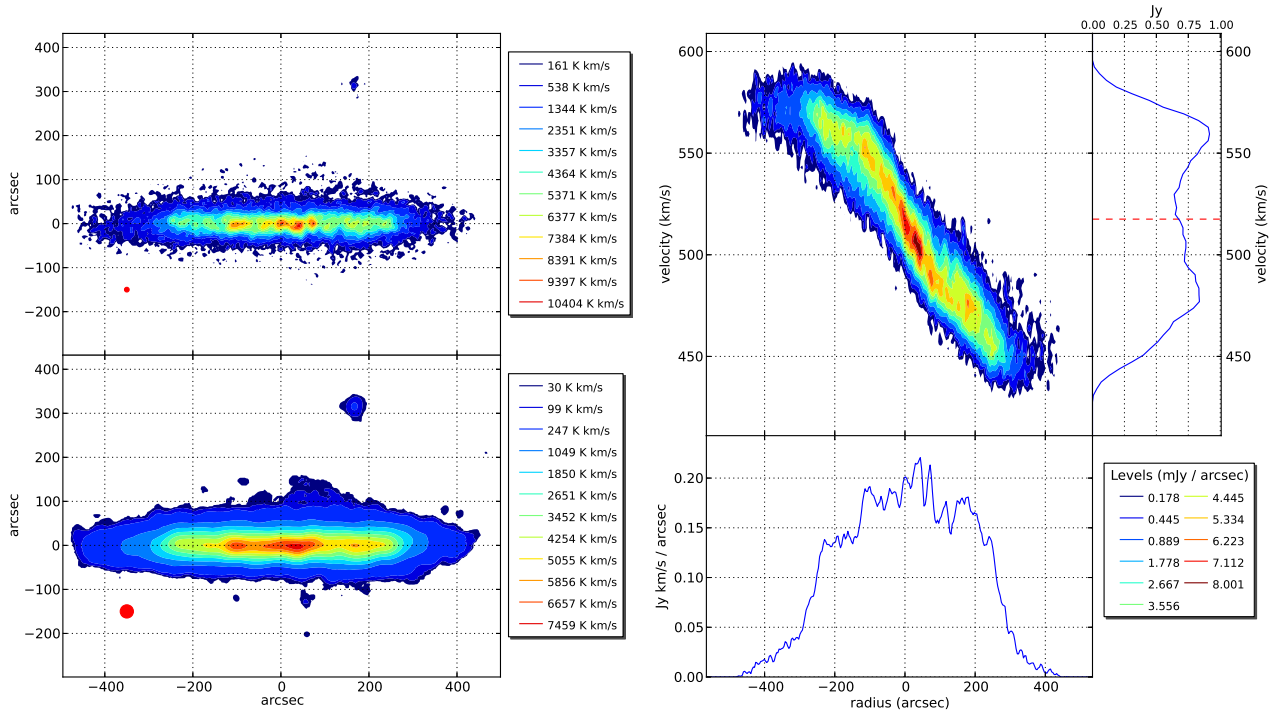
(d) Top-left plot shows the PV diagram. Contour levels are chosen at 2, 5, 10, 20, 30, 40, 50, 65, 80 and 95% of the maximum value, as shown in the legend. Right-top plot shows the integrated flux per velocity. The red dashed line shows v_{sys} . The lower plot shows the integrated flux per position along the major axis.

Fig. 6: Results for IC 5249



(a) DSS1 image overlaid with contours from the HI moment 0 map. Contour levels are spaced equally between the clipvalue and 95% of the maximum.

(b) Top plot shows the maximum temperature along v . Contours are equally spaced between the $2 \times \sigma$ and $T_{\max} - 10$ K. The middle plot shows the maximum temperature along z with the same color scaling. The lower plot maximum temperature along v and z and shows the inferred self-absorption for that position, assuming a spin temperature of 125 K.



(c) Top plot shows the moment 0 for the high resolution cube. Lower plot shows the moment 0 for the low resolution cube. Contour levels are spaced equally between the clipvalue and 95% of the maximum for that cube.

(d) Top-left plot shows the PV diagram. Contour levels are chosen at 2, 5, 10, 20, 30, 40, 50, 65, 80 and 95% of the maximum value, as shown in the legend. Right-top plot shows the integrated flux per velocity. The red dashed line shows v_{sys} . The lower plot shows the integrated flux per position along the major axis.

Fig. 7: Results for ESO 115-G021

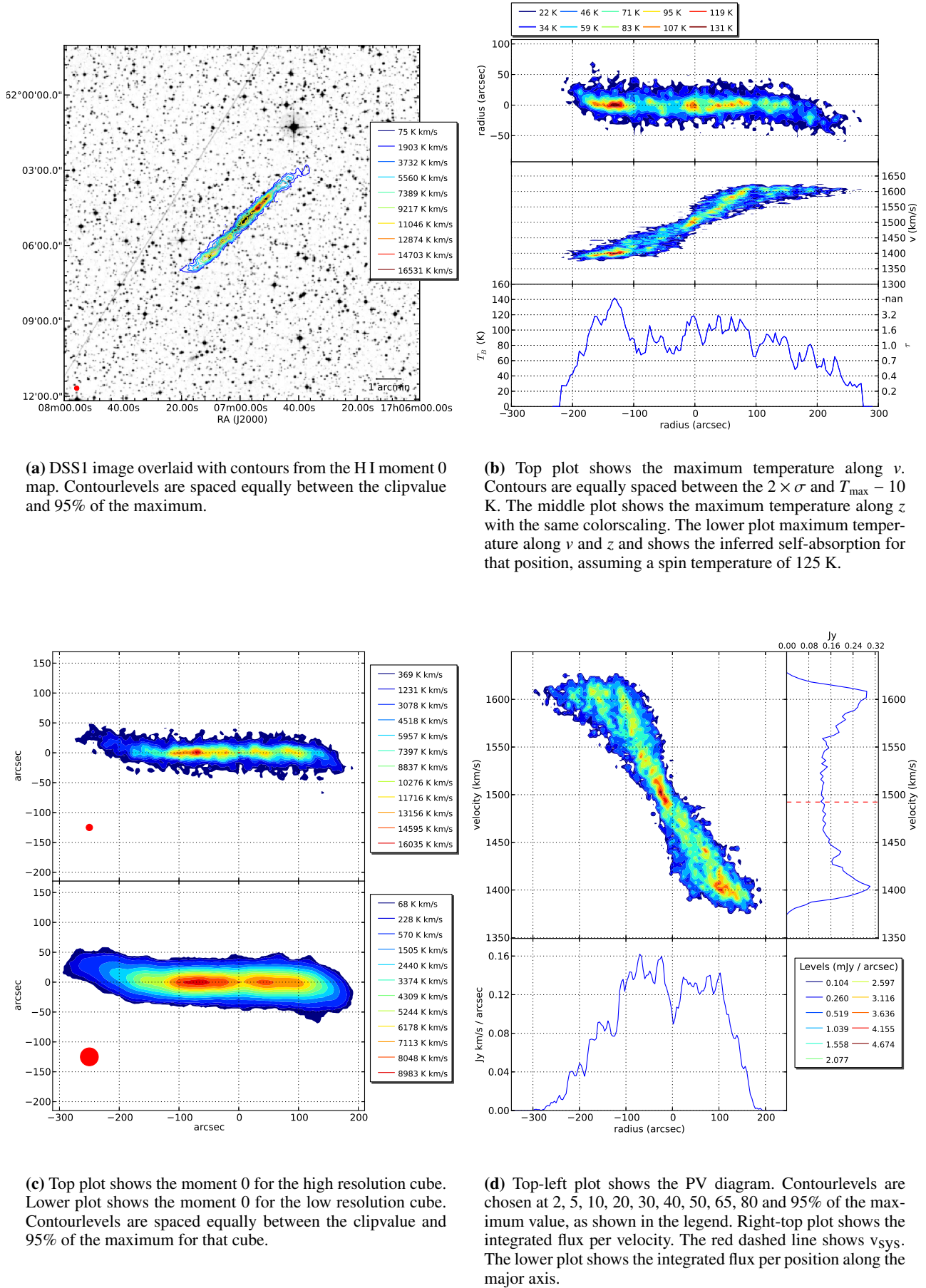


Fig. 8: Results for ESO 138-G014

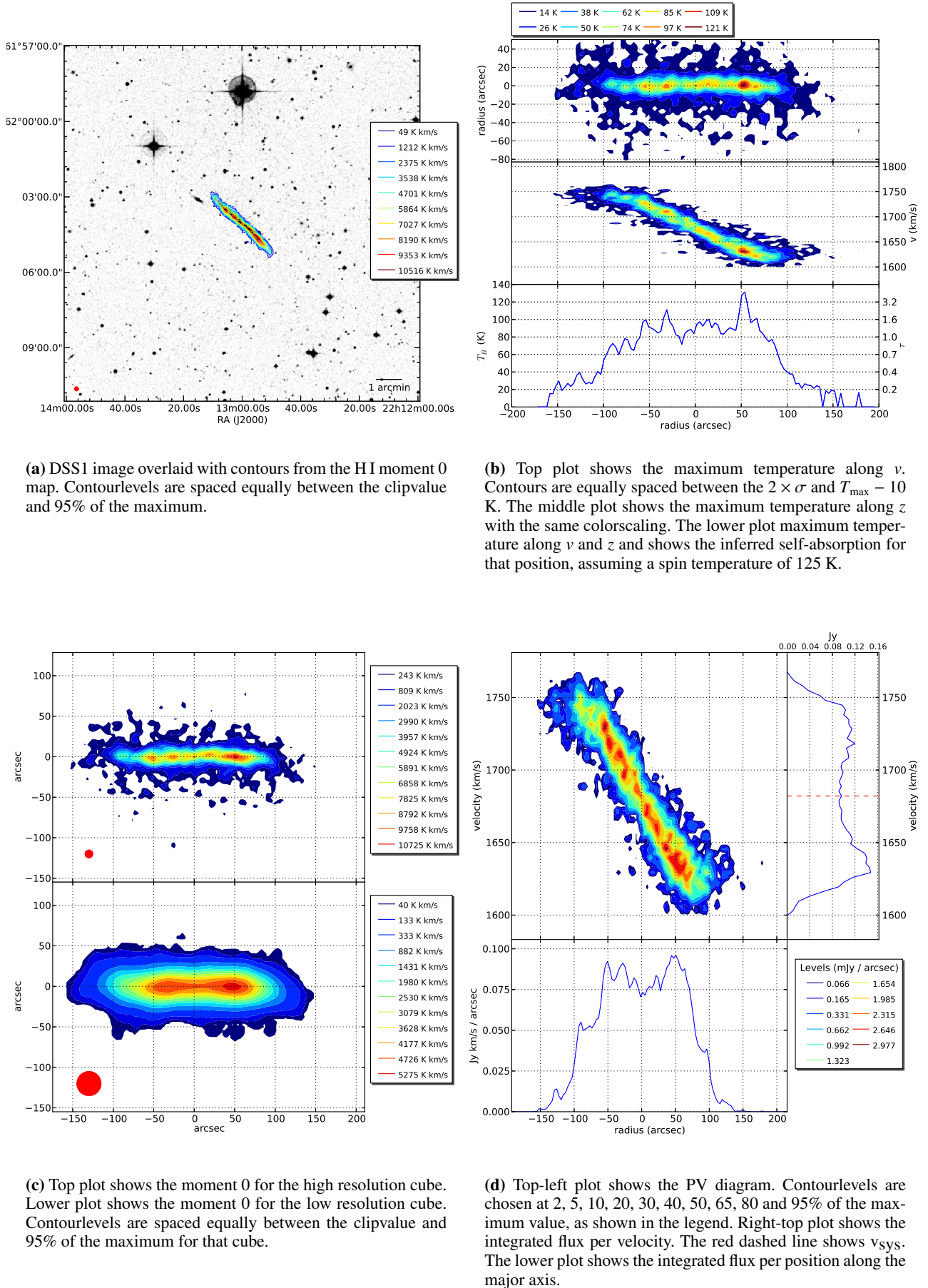
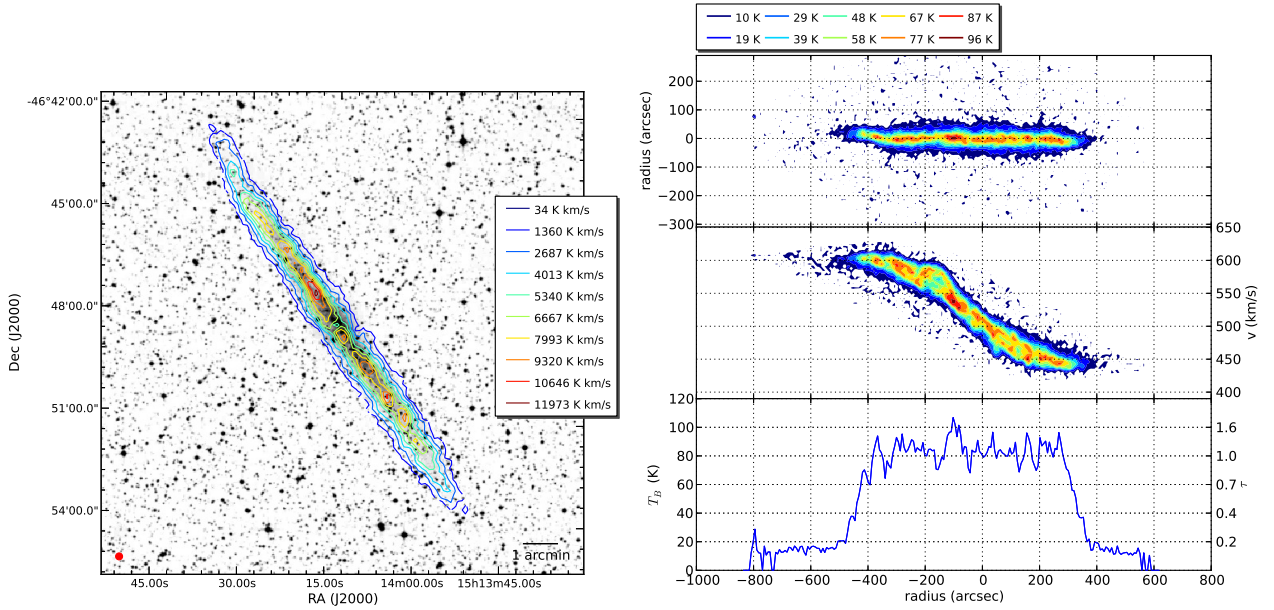
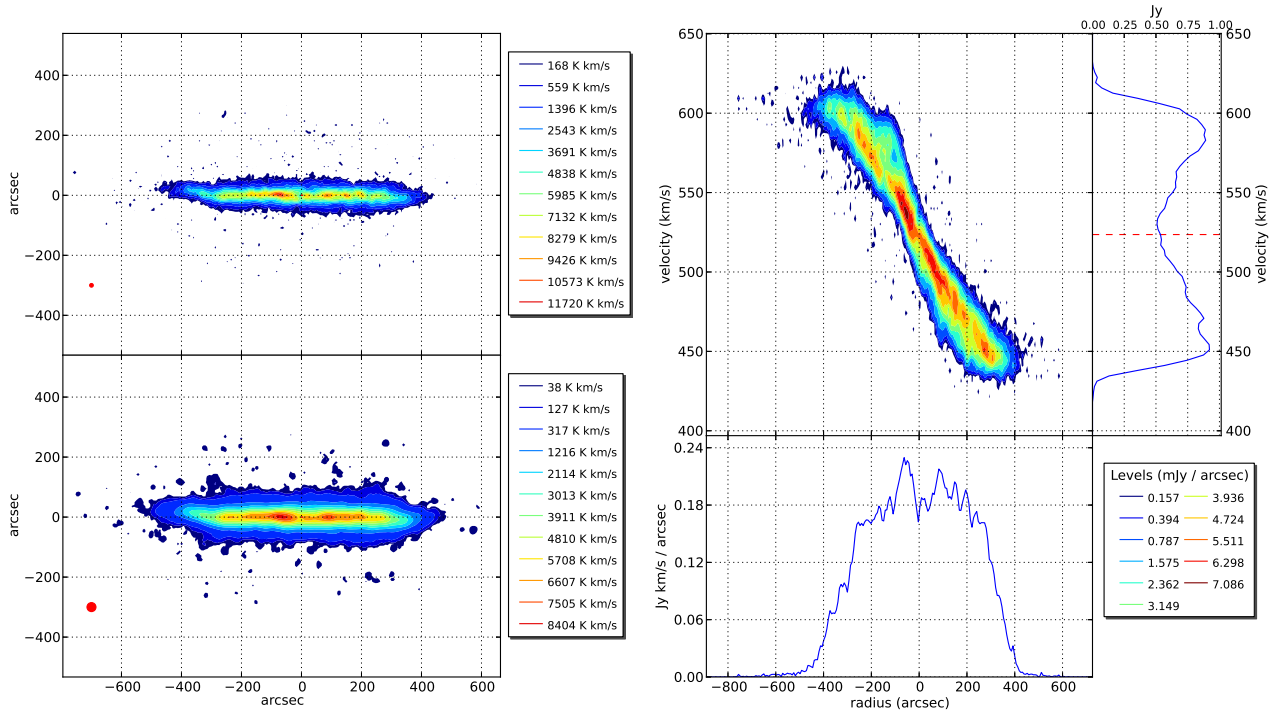


Fig. 9: Results for ESO 146-G014



(a) DSS1 image overlaid with contours from the HI moment 0 map. Contourlevels are spaced equally between the clipvalue and 95% of the maximum.

(b) Top plot shows the maximum temperature along v . Contours are equally spaced between the $2 \times \sigma$ and $T_{\text{max}} - 10$ K. The middle plot shows the maximum temperature along z with the same colorscaling. The lower plot maximum temperature along v and z and shows the inferred self-absorption for that position, assuming a spin temperature of 125 K.



(c) Top plot shows the moment 0 for the high resolution cube. Lower plot shows the moment 0 for the low resolution cube. Contourlevels are spaced equally between the clipvalue and 95% of the maximum for that cube.

(d) Top-left plot shows the PV diagram. Contourlevels are chosen at 2, 5, 10, 20, 30, 40, 50, 65, 80 and 95% of the maximum value, as shown in the legend. Right-top plot shows the integrated flux per velocity. The red dashed line shows v_{sys} . The lower plot shows the integrated flux per position along the major axis.

Fig. 10: Results for ESO 274-G001

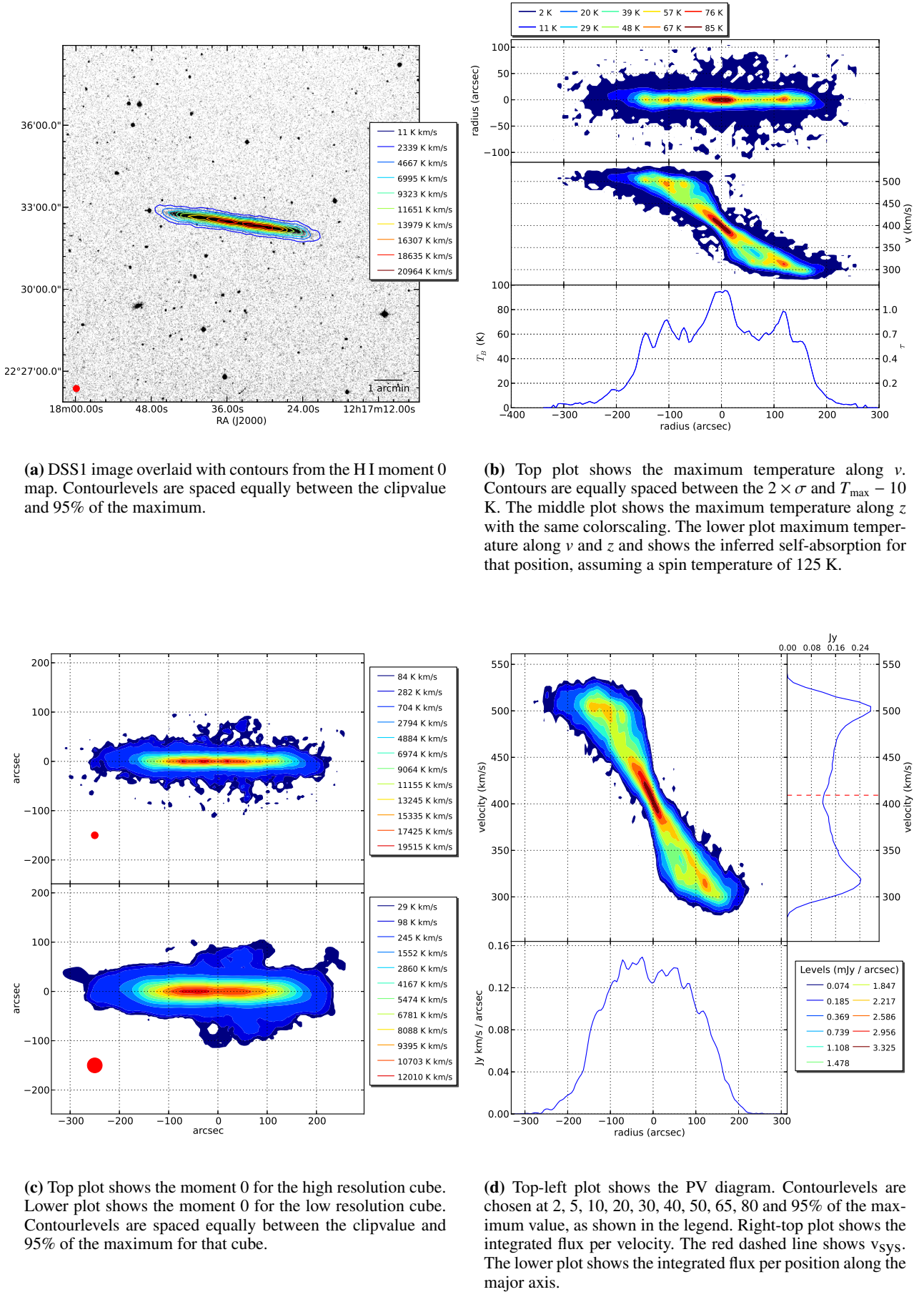


Fig. 11: Results for UGC 7321

Table 4: Details of the HI observations

Galaxy	Date	Telescope	Array	Project ID	Observer	Integration time (hr)
IC 2531	17-10-1992	ATCA	6C	C212	Carignan	7.5
IC 2531	06-04-1996	ATCA	6A	C529	Bureau	9.9
IC 2531	13-09-1996	ATCA	6B	C529	Bureau	10.0
IC 2531	07-03-1997	ATCA	1.5D	C529	Bureau	9.1
IC 2531	12-01-2002	ATCA	750A	C894	O'Brien	9.4
IC 2531	17-01-2002	ATCA	750A	C894	O'Brien	1.9
					Total:	47.7
IC 5052	17-10-1992	ATCA	6C	C212	Carignan	9.9
IC 5052	11-02-2001	ATCA	375	C934	Ryan	1.6
IC 5052	13-04-2001	ATCA	750D	C934	Ryan	1.9
IC 5052	25-02-2002	ATCA	1.5A	C894	O'Brien	6.7
IC 5052	01-12-2002	ATCA	6A	C894	O'Brien	10.5
IC 5052	03-02-2003	ATCA	750D	C894	O'Brien	2.5
IC 5052	18-04-2005	ATCA	1.5A	CX086	Dahlem	1.4
IC 5052	19-04-2005	ATCA	750A	CX086	Dahlem	5.7
IC 5052	23-04-2005	ATCA	750A	CX086	Dahlem	2.8
IC 5052	07-06-2005	ATCA	EW367	C1341	Koribalski	9.0
IC 5052	08-06-2005	ATCA	EW367	C1341	Koribalski	1.3
IC 5052	15-06-2005	ATCA	6B	CX086	Dahlem	3.8
IC 5052	09-07-2005	ATCA	H75	C1341	Koribalski	0.5
IC 5052	12-07-2006	ATCA	750B	C1341	Koribalski	11.3
IC 5052	20-11-2006	ATCA	1.5B	C1341	Koribalski	6.7
					Total:	75.5
IC 5249	18-10-1992	ATCA	6C	C212	Carignan	11.1
IC 5249	14-12-2002	ATCA	6A	C894	O'Brien	6.2
IC 5249	28-11-2002	ATCA	6A	C894	O'Brien	13.4
IC 5249	03-02-2003	ATCA	750D	C894	O'Brien	8.0
IC 5249	20-03-2003	ATCA	EW352	CX043	Dahlem	0.6
IC 5249	21-03-2003	ATCA	EW352	CX043	Dahlem	1.6
IC 5249	22-03-2003	ATCA	EW352	CX043	Dahlem	0.4
					Total:	41.2
ESO 115-G021	07-10-1993	ATCA	1.5D	C073	Walsh	0.9
ESO 115-G021	22-05-1995	ATCA	1.5B	C073	Walsh	1.7
ESO 115-G021	23-06-1995	ATCA	750B	C073	Walsh	7.0
ESO 115-G021	08-09-2002	ATCA	6C	C894	O'Brien	6.5
ESO 115-G021	03-12-2002	ATCA	6A	C894	O'Brien	10.1
ESO 115-G021	13-12-2002	ATCA	6A	C894	O'Brien	5.7
ESO 115-G021	16-01-2005	ATCA	750B	C1012	Hoegaarden	11.2
ESO 115-G021	09-02-2005	ATCA	EW352	C1341	Koribalski	10.1
ESO 115-G021	09-07-2005	ATCA	H75	C1341	Koribalski	0.6
ESO 115-G021	24-11-2005	ATCA	1.5C	C1341	Koribalski	9.3
ESO 115-G021	31-01-2006	ATCA	750D	C1341	Koribalski	10.3
ESO 115-G021	11-01-2009	ATCA	6C	C1341	Koribalski	10.1
					Total:	83.5
ESO 138-G014	08-11-2002	ATCA	1.5A	C894	O'Brien	10.4
ESO 138-G014	29-11-2002	ATCA	6A	C894	O'Brien	9.8
ESO 138-G014	10-03-2011	ATCA	1.5A	C2422	Peters	5.0
					Total:	25.2
ESO 146-G014	27-12-2000	ATCA	750C	C894	O'Brien	10.4
ESO 146-G014	11-01-2001	ATCA	750C	C894	O'Brien	1.6
ESO 146-G014	31-07-2001	ATCA	1.5A	C894	O'Brien	7.6
ESO 146-G014	17-01-2002	ATCA	750A	C894	O'Brien	1.4
ESO 146-G014	27-01-2002	ATCA	6B	C894	O'Brien	10.5
ESO 146-G014	14-04-2002	ATCA	6A	C894	O'Brien	10.2
					Total:	41.7
ESO 274-G001	29-08-1993	ATCA	1.5B	C073	Walsh	5.8
ESO 274-G001	07-10-1993	ATCA	1.5D	C073	Walsh	6.5
ESO 274-G001	28-11-2002	ATCA	6A	C894	O'Brien	9.6
ESO 274-G001	23-02-2006	ATCA	EW367	C1341	Koribalski	8.1
ESO 274-G001	15-06-2006	ATCA	1.5D	C1341	Koribalski	10.2
ESO 274-G001	08-10-2006	ATCA	H75	C1341	Koribalski	5.0
ESO 274-G001	23-01-2007	ATCA	750A	C1341	Koribalski	10.1
ESO 274-G001	18-01-2011	ATCA	6.0A	C2422	Peters	1.6
ESO 274-G001	11-03-2011	ATCA	1.5B	C2422	Peters	9.8
					Total:	66.9
UGC 7321	26- & 30-05-2000	VLA	C	AM649	Matthews	16.0
					Total:	16.0